

Simulation of thermal and mechanical performance of laser cladded disc brake rotors

Nicholas Athanassiou^{1,2} , Ulf Olofsson², Jens Wahlström³ 
and Senad Dizdar²

Proc IMechE Part J:
J Engineering Tribology
2022, Vol. 236(1) 3–14
© IMechE 2021



Article reuse guidelines:

sagepub.com/journals-permissions

DOI: 10.1177/13506501211009102

journals.sagepub.com/home/pij



Abstract

Disc brakes wear during braking events and release airborne particulates. These particle emissions are currently one of the highest contributors to non-exhaust particle emissions and introduce health hazards as well as environmental contamination. To reduce this problem, wear and corrosion-resistant disc coatings have been implemented on grey cast iron brake disc rotors by using various deposition techniques such as thermal spraying and overlay welding. High thermal gradients during braking introduce risks of flaking off and cracking of thermally sprayed coatings with adhesive bonding to the substrate. Overlay welding by laser cladding offers metallurgical bonding of the coating to the substrate and other benefits that motivate laser cladding as a candidate for the coating of the grey cast iron brake discs. This study aims to investigate the effect of laser cladding on the thermal and thermo-structural performance of the coated grey cast iron brake discs. Therefore, thermal and thermo-stress analysis with COMSOL Multiphysics 5.6 software is performed on braking events of grey cast iron brake discs as non-coated – reference and laser cladding coated with stainless steel welding consumables. The Results demonstrated that surface temperatures were more localised, overall higher in the laser cladded coating with over three times the stresses attained of reference grey cast iron discs. The output of the simulations has been compared by tests found in the literature. Laser cladding presented higher reliability and braking performance, nonetheless requiring the evaluation of its thermal impact on other system components.

Keywords

laser cladding, coating, grey cast iron, disc brakes, friction, thermal stress, thermal performance

Date received: 1 December 2020; accepted: 13 March 2021

Introduction

Braking systems aim to controllably reduce the velocity of a body in motion, or completely stop it. In the case of vehicles, braking is constituted by a torque applied in the opposite direction to a wheel's motion. This is done so through frictional contact in the tribological pad–disc interface, where a brake pad made of friction material applies pressure on the brake rotor surface. The kinetic energy is then transformed into thermal energy due to friction which, therefore, decelerates the vehicle. The dilemma which accompanies a braking action is, however, the consequence of particle emission. In the debris of worn material surfaces, particulate matter (PM) in the micrometre scale becomes airborne,¹ introducing a severe contamination hazard in urban environments known as non-exhaust emission (NEE).² These PMs originate in tyre wear, road surface wear, road dust resuspension and finally, brake pad and brake disc wear.¹

Air pollution has received an extensive focus throughout the last few decades from the European Union and the

World Health Organisation (WHO). Much of the work has, however, been inclined towards ‘exhaust’ emissions instead, with hardly any legislation implemented for NEE.² This has left NEE with very little development, letting it contribute enough to reach almost half of road vehicle full-scale emissions.¹ As more sustainable vehicles are released on the market such as hybrid or electric cars, the dominating impact gradually begins to shift to NEE. In order to mitigate the issue of airborne PM, many techniques have been implemented. These include hardening, high-velocity oxygen fuel³ or high-velocity

¹School of Engineering, King's College, University of Aberdeen, UK

²Department of Machine Design, KTH Royal Institute of Technology, Stockholm, Sweden

³Department of Mechanical Engineering, Lund University, Sweden

Corresponding author:

Nicholas Athanassiou, School of Engineering, King's College, University of Aberdeen, Aberdeen AB24 3UE, UK.

Email: nicholas.athn@gmail.com

air fuel for thermal sprays, powder welding, atmospheric plasma or flame spraying.⁴ All of these offer a range of material deposition on substrates along with different forms of bonding techniques. Nevertheless, challenges, such as crack formations and flaking of coated layers, have demonstrated to occur during braking events.³

Among other coating technologies, laser cladding (LC; also known as laser metal deposition) by using metal powder welding consumables offers metallurgical bonding of the coating to the substrate, high purity of coating, very low porosity level⁵ and quite small thermal deformations of the substrate. It has been proven through pin-on-disc wear testing comparisons with a grey cast iron (GCI) disc that an LC Ni/carbide coating mass wear is halved, specific wear loss is quartered while there was no 'substantial increase' in wear from the pin neither.⁶ Further, 30% of particle emission concentration is reduced, with an approximate half in 'size partition of particles below 7 μm '.⁶ These beneficial results demonstrate that a significant reduction in wear emission can be achieved.

Thermal stress performance highly governs the compatibility and adhesion strength of coatings. Crack formations and flaking are consequences of thermal stresses, which surpass the coating adhesion bonding strength to the substrate.⁵ A degree of expansion results from the increase in temperature of a rotor subject to braking conditions. When a rotor is non-homogeneous (as in the case of coatings), thermal expansion differences mean high thermal stresses are developed at the materials interface.⁷ Consequently, the coating adhesion with the substrate is at risk of failure.

Various simulation techniques have been implemented in previous studies to predict thermal and stress performances of disc brakes. The variation in these methods is mainly governed by the scale of the analysis. This is relevant for example, on the mesoscopic scale, where a cellular automation approach developed by Müller and Ostermeyer⁸ was used to predict plateau dynamics. The literature demonstrates that the effect of mesoscopic contact on macroscopic scales can be simulated numerically with time and length orders of magnitude specified by Wahlström.⁹ As this study conducts a physics coupling finite-element analysis (FEA), it is also interesting to refer to Pan and Cai,¹⁰ who demonstrate that heat flux due to friction can be translated into an area subject to a direct heat rate. The literature gap however lays in the fact that no research has been done to simulate the above-mentioned mechanical performance relevant to coated disc models.

The aim of the present work is to investigate the effect of LC coating of GCI brake disc rotors on the discs' thermal and thermo-structural performance. This is done by simulation of the braking event for reference GCI – and LC-coated rotors by using COMSOL Multiphysics 5.6 simulation software. Regarding thermal stresses, this is highly relevant for the evaluation of predicted LC compatibilities under braking conditions. Stress magnitudes can be anticipated before the deposition process takes place, in order to establish a degree of bonding tolerance.

Method

In the present work, an FEA study was conducted to simulate a dyno bench test environment. This allowed for the validation process of the model, which represented a conventional uncoated (or homogeneous) GCI brake disc, simulated under the same conditions as the dyno performed by Wahlström.⁹ A laser cladded coating was added to the same model subject to simulation, in order to identify clear comparisons. A physics coupling interface software was used in order to combine both heat transfers in solids with solid mechanics hence, able to obtain thermal stress data. These are obtained by firstly importing a computed temperature field model.¹⁰ This is obtained through an FEA study performed by the implementation of a heat source, representing a frictional heat flux. The thermal implementation is specified as a region where the inward heat flux is directly acting, as opposed to specifying the sweeping commands of a frictional heat source.¹¹ Thermal data is then, automatically fed back into the study through a coupled software interface to compute thermal stress values.

The applied pressure on the rotor in the dyno test is a known parameter, which by multiplying by the pad contact area, determines the normal force applied. The need for calculating the inertial load received by the front vehicle axle dependent on its deceleration is therefore eliminated.⁹ This facilitates the computation greatly given that only one simple expression must be specified. If we begin by stating the braking power as stated in equation (1)¹⁰ that the disc receives $P_{b,disc}$ (W), we obtain:

$$P_{b,disc} = v_{slip} F_f \xi \quad (1)$$

where v_{slip} (m/s) is the slip velocity of the rotor, which relates to the same angular velocity, ω (rad/s) as the vehicle wheel times a given radius on the disc, r (m), F_f (N) is the frictional (or tangential) force and ξ is the heat partition coefficient, which estimates the proportion of heat generated in the disc as opposed to the pad, $Q_{disc} = \xi Q_{total}$ (typically in the range of 98%–99%). This coefficient is suggested by Vernotte,¹² which considers the thermal properties of each material:

$$\xi = \frac{S_d \sqrt{\alpha_d C_{p,d} k_d}}{S_d \sqrt{\alpha_d C_{p,d} k_d} + S_p \sqrt{\alpha_p C_{p,p} k_p}} \quad (2)$$

where S_d (m^2) is the contact surface area of the disc, S_p (m^2) is the contact surface area of the pad, α_d is the thermal expansion coefficient of the disc, α_p is the thermal expansion coefficient of the pad, $C_{p,d}$ (J/(K · kg)) is the specific heat capacity of the disc, $C_{p,p}$ (J/(K · kg)) is the specific heat capacity of the pad, k_d (W/(m · K)) is the thermal conductivity of the disc and k_p (W/(m · K)) is the thermal conductivity of the pad. The slip velocity can be represented as the ratio between the wheel radius, R (m), and a given radius on the disc, r (m), of the vehicle velocity, v (m/s):

$$v = R\omega, \quad \omega = \frac{v}{R} \quad (3)$$

$$v_{\text{slip}} = r\omega = r\frac{v}{R}, \quad v_{\text{slip}} = \frac{r}{R}v \quad (4)$$

The dependency with time, t (s), of the slip velocity is related by $\omega(t) = \omega_0 + \alpha t$, where ω_0 (rad/s) is the initial angular velocity and α (rad/s²) is the angular acceleration. In order to take into account a geometrical dependency, a more accurate slip velocity can be specified as follows:

$$\begin{aligned} r_{x,y}\omega(t) &= \sqrt{v_x^2 + v_y^2} = \sqrt{(x\omega(t))^2 + (y\omega(t))^2} \\ &= \omega(t)\sqrt{x^2 + y^2} \end{aligned} \quad (5)$$

where $r_{x,y}$ (m) is the radius from the centre of the disc to any two-dimensional (2D) point with coordinates (x, y) on its surface; v_x (m/s) is the slip velocity in the x -direction and v_y (m/s) is the slip velocity in the y -direction. By substituting the definition of the frictional force $F_f = \mu F_N$, we obtain the final implemented expression for the frictional heat rate $Q_{b,\text{disc}}$ (W/m²), where μ is the coefficient of friction and F_N (N) is the normal force applied from the pad onto the disc:

$$P_{b,\text{disc}} = \omega(t)\sqrt{x^2 + y^2}\mu F_N \xi \quad (6)$$

$$Q_{b,\text{disc}} = \frac{P_{b,\text{disc}}}{A} \quad (7)$$

This derived expression is verified thanks to Pan and Cai,¹⁰ who also proposed this expression to be implemented with the assumption that ‘friction heat is directly exerted to the surface of the brake disc’.¹⁰ Once this is used as a command during the software configuration, the system represents a temperature field applied in the form of a regional heat source instead of directly being generated due to friction. Consequently, the derivation has greatly simplified the input expressions and facilitates the conciseness of the expected results. Its simplicity however does not jeopardise the accuracy of local heat fluxes within the model geometry. This is due to the allowance of 2D point coordinates and time evolution for slip velocity specifications directly affecting the heat rate.

Simulation specimens and materials

The proposed coating application consists of a nickel-based alloy buffer layer, with a martensitic stainless steel overlayer. These are deposited on a GCI substrate as the core material of the brake disc. Regarding material data, an approximation is made with a nickel-based alloy type Inconel 718,¹³ and martensitic stainless steel type AISI 420.¹⁴

Martensitic stainless steels in general offer relatively high hardness, moderate to high wear resistance and moderate to good corrosion resistance.¹⁴ The function of the interface layer is twofold to act as a corrosion barrier by sealing the GCI rotor from potentially infiltrated moisture and other corrosive agents, and to prevent dilution of

Table 1. Material properties for rotor sections. Grey cast iron, Inconel 718 and AISI 420 refer to the disc substrate, interlayer and overlayer respectively.

Material property	Grey cast iron ⁹	Inconel 718 ¹³	AISI 420 ¹⁴
Density (kg/m ³)	7850	8220	7800
Young's modulus (GPa)	98	200	200
Poisson's ratio	0.27	0.29	0.28
Thermal expansion coefficient (μK ⁻¹)	11	13	11
Thermal conductivity (W / (m · K))	50	11	16
Specific heat capacity (J / (K · kg))	500	435	460

graphite from the substrate material with the martensitic stainless steel surface coat. This dilution would occur during LC of the martensitic steel overlay over bare GCI surface and substantially lower the quality of the cladding. However, by having a nickel-based alloy buffer layer with virtually no chemical affinity to carbon as opposed to martensitic stainless steel, the dilution is suppressed. Lower heat infiltration into the disc core is also achieved given that this interface layer acts as a thermal barrier that traps most of the heat at the surface of the coating. Following in Table 1 are the listed parameters representing relevant material properties implemented in the study.

Implementation

The chosen FEA software is COMSOL Multiphysics 5.6. Other than its simplicity of use and the straightforwardness of configuration commands, the software provides the possibility of coupling different physics that are needed to be analysed, through a Multiphysics command. The benefit of this option associated with this study is the analysis of both heat generation in a disc brake rotor and its associated thermal stresses. Downsides include computational cost, which is why it is crucial to retail a simplified model¹⁵ for mesh independence. Figure 1 displays the simulation routine implemented in the study.

Each routine was repeated for each model: GCI and LC. These consist of an identical geometry distinguished purely by the two 150 μm layers added on the LC model surface. Both layers represent the coating that an LC process would deposit on a substrate surface. Moreover, an LC surface texture has shown similar surface topography to that of GCI from the literature.⁶ Results demonstrate that they are mainly distinguished by the fact that LC holds approximately three times the surface hardness of GCI (<20 HRC, whereas 58 HRC for LC).⁶ This is expected from the level of debris reduction that has been investigated,⁶ however, plays an insignificant role in thermal and mechanical FEA comparison.¹¹ Hence, this justifies that surfaces of each model may be

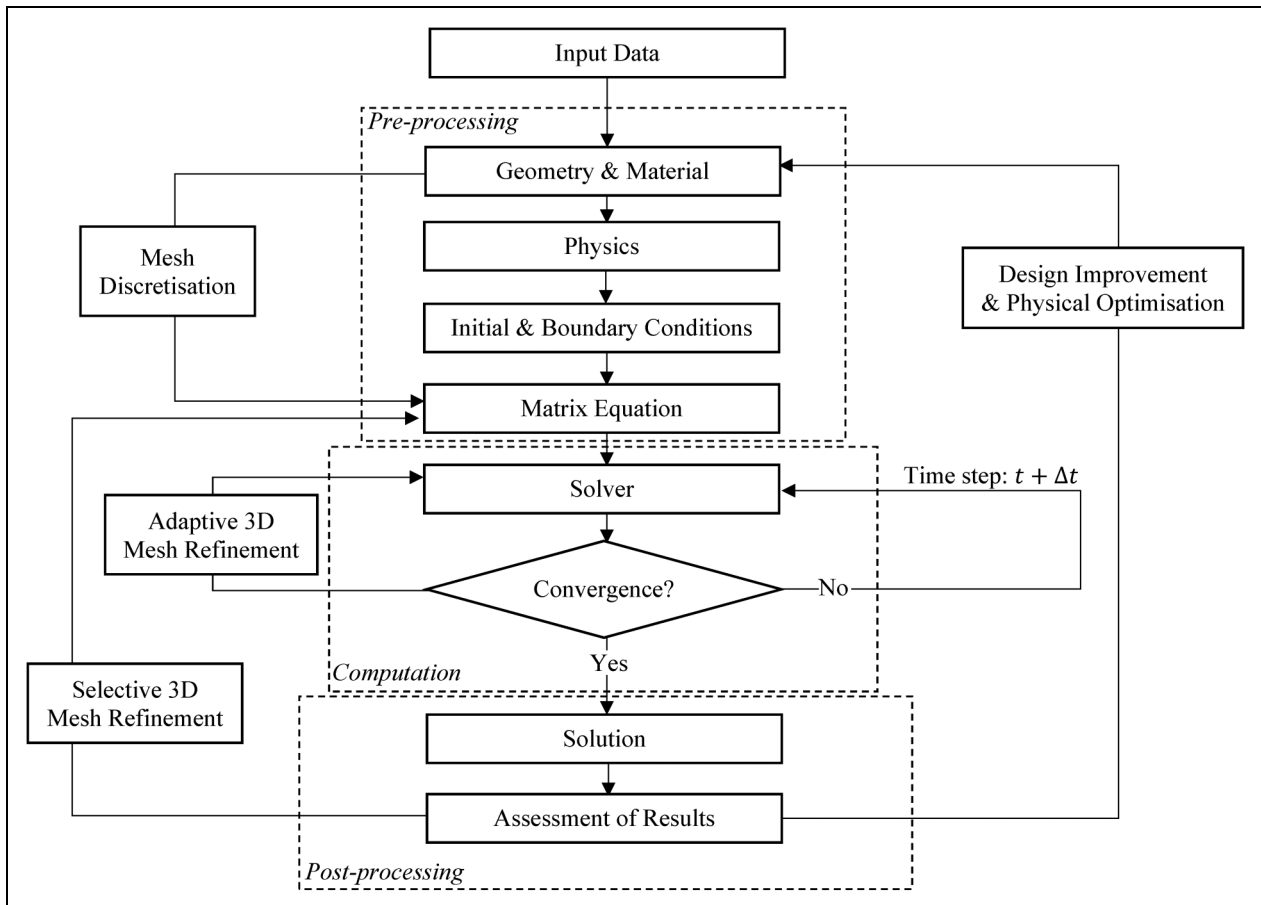


Figure 1. Overview of simulation routine.

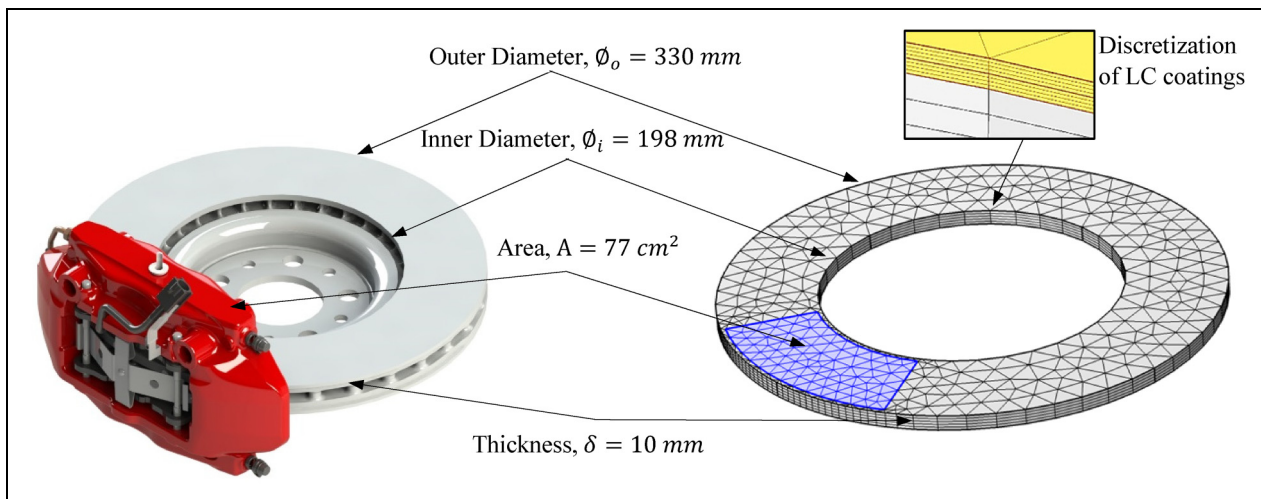


Figure 2. Disc brake assembly rendered on SolidWorks (left), finite-element analysis (FEA) disc model designed on COMSOL (right).

assumed to have the same surface topography and therefore, only distinguished by their friction coefficients.⁶

Furthermore, a 10 mm thick solid disc is used, representing each contact section of the full ventilated rotor. The interior of the disc is removed to match the geometry of the original model presented in Figure 2. This also aims at reducing the total number of discretisation elements of the model and hence, computational cost. Dyno bench test

conditions are as follows.⁹ The pads apply a normal force on each contact face of the rotor. This is determined from the pressure applied through the hydraulics and the pad-disc nominal contact area ($= 77\text{ cm}^2$). The braking scenario simulates a braking event, where a 1702 kg vehicle decelerates from 180 to 80 km/h with a deceleration of 0.5 g .⁹ As the wheel radius is known to be 295 mm, the initial and final angular velocities of the

wheel are determined. The kinematics therefore represent a linear deceleration of 16.6 rad/s^2 between 170 and 75 rad/s , leading to a braking time of 5.7 s . A mean coefficient of friction value of 0.4 is chosen for the GCI model, retrieved from experimental data using a dynamometer bench test.⁹ A mean friction coefficient value of 0.6 is chosen instead for a laser clad surface, retrieved from experimental data involving a pin-on-disc tribometer within a particle emission testing cell.⁶ The full disc is selected to undergo an angular velocity of $\omega(t)$, where $\omega(t) = \omega_0 + at$. When multiplied by the modulus of the x and y coordinates for a given point among the disc surface, this will calculate the according slip velocity (increasing linearly as the outer radius is approached). Two $150 \mu\text{m}$ layers are added on the top surface of the disc with the pad sketched on the top surface for LC. Following in Figure 2 is the simulation model (right of the figure) where the highlighted region represents the boundary where the heat flux enters the disc body. As well as this a three-dimensional (3D) computer-aided design (CAD) model of the disc brake assembly tested under the dyno bench test is displayed (left of the figure).

Each domain (bulk, interface and surface layer) is specified with its according material properties as specified in Table 1. The translational motion is specified as a local disc velocity vector $v_d = \frac{v}{R}(-y, x)$. This can be also rewritten as $-y\omega(t) \text{ m/s}$ for the x -plane and $x\omega(t) \text{ m/s}$ for the y -plane, which specifies a counter-clockwise rotation. Initial conditions are set to 100°C for the full model in order to recreate the measured data in the dyno test which allowed the disc to cool down to a minimum of 100°C before beginning a new braking cycle.⁹ The expression used for the retardation power during the dyno bench test is described as an 'if' function specifying that there exists a heat input purely between $t = 0$ and $t = \frac{\omega_i - \omega_f}{\alpha}$ as the time it takes for the disc to decelerate from the initial to final angular velocities, ω_i and ω_f ($\sim 5.7 \text{ s}$). This power is then divided by the nominal contact area (77 cm^2 computationally measured from an integral of the contact boundary) to calculate the heat rate. Coefficients of heat partition with the brake pad for the GCI and martensitic stainless steel are equal to 0.98 and 0.97 , respectively (calculated using equation (2)). The friction force, μF_{normal} is fixed for both models for consistency. Regarding GCI, $\mu_{\text{GCI}} F_{\text{normal_GCI}} = 0.4 \times 10.4 \text{ kN}$, taken from the dynamometer test.⁹ However, the LC surface holds a higher coefficient of friction (of value 0.6) which, for a same normal force applied (10.4 kN) would result in a higher friction force. Consequently, for an increase in friction coefficient, there must be a proportional decrease in normal force applied, in order to reach the same braking performance (or vehicle deceleration). The product is adjusted as follows, where μ_{GCI} and μ_{LC} are the friction coefficients and $F_{\text{normal_GCI}}$ and $F_{\text{normal_LC}}$ are the normal applied forces for GCI and LC, respectively. The adjusted normal force applied for LC is the ratio between friction coefficients times the GCI normal force applied:

$$\mu_{\text{GCI}} F_{\text{normal_GCI}} = \mu_{\text{LC}} F_{\text{normal_LC}} \quad (8)$$

$$F_{\text{normal_LC}} = \frac{\mu_{\text{GCI}}}{\mu_{\text{LC}}} F_{\text{normal_GCI}} \quad (9)$$

Forced and natural convective heat transfer coefficients of 70 and $9 \text{ W/m}^2\text{K}$, respectively, were reported in the dyno bench test⁹ for an ambient temperature $T_{\text{air}} = 300 \text{ K}$. Surface emissivity is set to 0.95 and 0.2 for GCI and LC, respectively.

An adaptive mesh refinement iteration is made of 11 sequences, where the computation is physics controlled. As well as this for post-processing, a selective mesh refinement is made to obtain mesh independence in the required regions of interest. Finer meshing is implemented in regions of high expected thermomechanical gradients, hence in the influx boundary region of frictional heat,¹⁰ highlighted on the meshed model in Figure 2. Mesh refinement validation is achieved in three different regions of the model: the pad-to-disc contact, the region of circular sweep path of the pad and the disc thickness. The absolute percentage difference is brought down to $<1\%$ for each model, with every decrease in element size. Computational cost is hence minimised in exchange for the required accuracy of results.¹¹ A triangular mesh is established at the surface of the disc of the same fineness for both GCI and LC. Triangular elements are used given that results prove to follow experimental data with more comparable synchrony and magnitudes, as opposed to quadrilateral elements.¹⁵ The thickness of the disc is swept and distributed between initially, an equally sized number of elements as shown right of Figure 2 (a zoomed-in section of the LC discretised coating is displayed). It was however found that by setting a predefined symmetric elemental growth where element separations decrease as boundary domains are approached, mesh independence was achieved more effectively. The number of elements is varied until mesh independent results are observed throughout the LC interior. An element ratio of 20 is set in each coating thickness distributed between 20 elements symmetrically. The GCI substrate is set to an element ratio of 100 , where element separations decrease towards the interlayer and distributed between 40 elements. This configuration was found to optimise validation of the model, at the appropriate computational cost.

Hence, the combination of a 2D mesh (as triangular elements) with swept elements (along the disc thickness) instead of directly implementing 3D (tetrahedral) elements¹⁵ provides the following benefits: reduces mesh detail where it is not required and provides adjustable interior accuracy of the model. This plays a significant role especially for the LC simulation due to its fine surface geometry of the coating layers and delicate interface regions. Computational cost of the LC simulation is hence greatly reduced given that a 3D element geometry would significantly increase the total number of elements needed to fully discretise the model. The computation is run for time increments of 0.01 s ; a time range between 0 and 10 s ; for a braking cycle taking place between 0 and 5.7 s .

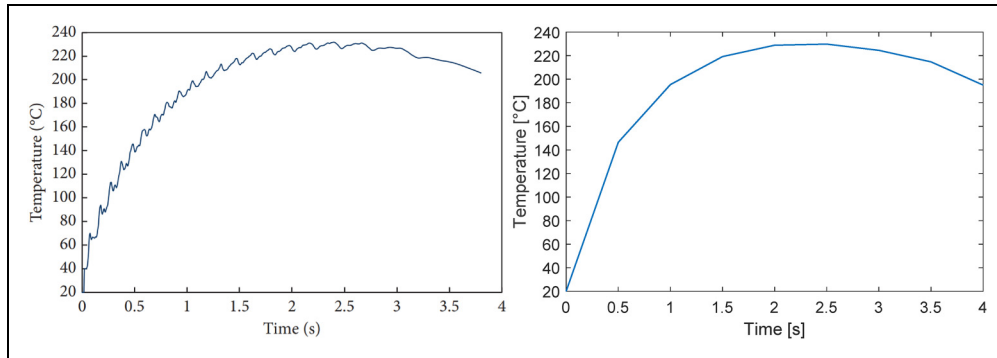


Figure 3. Temperature verification: Experimental temperature evolution retrieved from Pan and Cai¹⁰ (left), re-modelled COMSOL simulation (right).

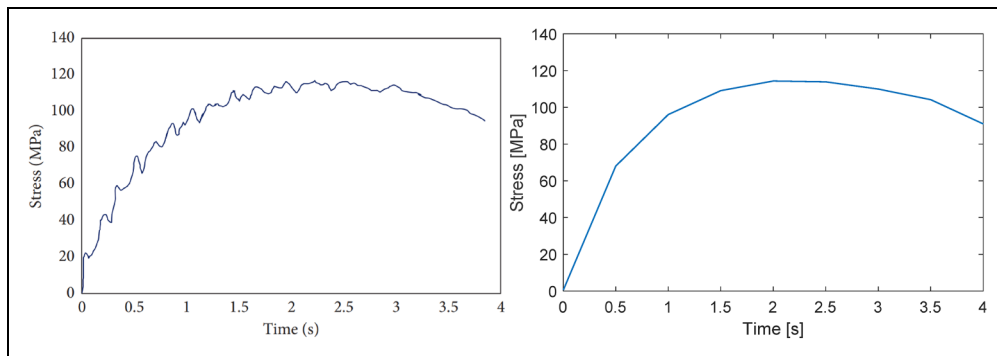


Figure 4. Thermal stress verification: Experimental thermal stress evolution retrieved from Pan and Cai¹⁰ (left), re-modelled COMSOL simulation (right).

Results

The first part displayed in this section presents the verification of temperature evolution and thermal stress evolution by comparison with results found in the literature. The second part presents thermal comparisons in the form of graphs as well as 3D temperature maps, followed by thermal stress comparisons also in the form of graphs and 3D thermal stress maps at LC coating interfaces.

Comparison with literature results

Physics validation was made with Pan and Cai's¹⁰ measured stresses from a dynamometer by recreating the described model with the provided parameters. These consisted of a disc outer radius, $R_o = 148$ mm; thickness, $\delta = 28$ mm; mean elastic modulus, $E = 95$ GPa; mean specific heat capacity, $C_p = 530$ J/(K · kg); mean thermal conductivity, $k = 43.1$ W/(m · K); mean friction coefficient, $\mu = 0.38$; and mean thermal expansion coefficient, $\alpha = 11.65$ μ /°C. The evolution of the angular velocity is obtained from: $\omega(t) = 66.87 - 17.47t$, for $0 \text{ s} \leq t \leq 4 \text{ s}$ and time steps are set to 0.5 s. Once temperature curves were successfully achieved, model constraints were applied in order to obtain a stress evolution. Figures 3 and 4 display the temperature and stress evolution comparison, respectively.

Results therefore demonstrate of being in line with literature data. This allows for verification of the GCI

model, given that results from the literature are obtained from a GCI disc brake rotor. The selective mesh refinement was followed for a temperature evolution along a line at the effective radius travelling all the way through the thickness of the disc. The effective radius is determined as the centre of mass (or nominal contact pressure) of the pad appliance onto the disc. The thickness of the disc was distributed with the above-mentioned mesh combination. The displayed temperature variation is selected at a time instant of $t = 1$ and 5 s of braking time.

Thermal analysis

The following plots display the heat evolution along the thickness line positioned vertically at the effective radius of the disc. This may be considered the disc thickness. The purpose of these results is beginning to evaluate how much heat is infiltrated into the disc and consequently, conserved in the LC coating. This data will then be fed back into the simulator to solve for solid mechanics of the model, in order to determine thermal stresses.

It is important here to take into account that these above plots from Figure 5 are the converged plots obtained from the iteration sequences previously performed for mesh independence. The plot for LC extends further due to the 0.3 mm total layer that is deposited on the 10 mm GCI substrate. Left of Figure 5 is the thermal

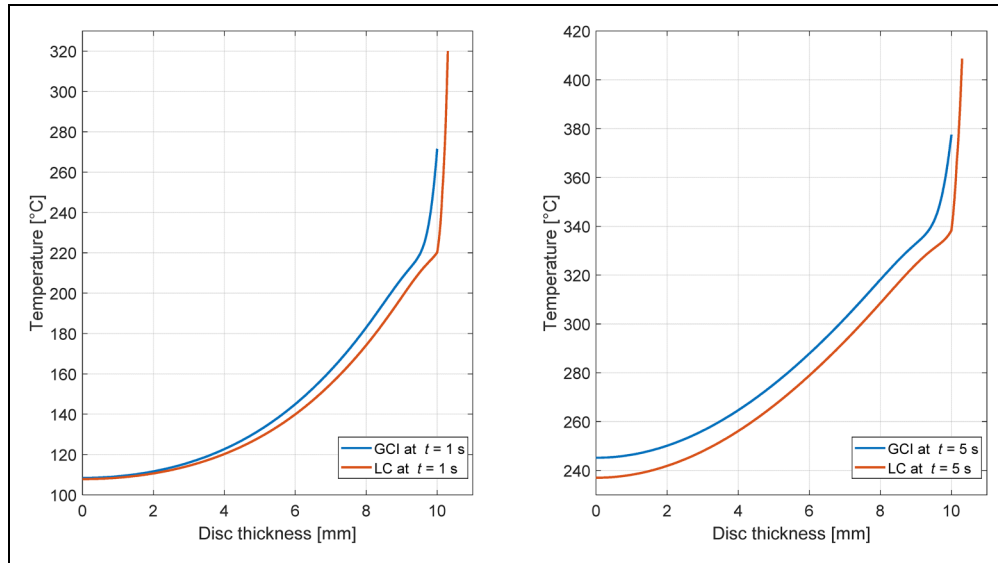


Figure 5. Temperature evolution along the disc thickness line. GCI and LC are presented after 1 s of braking (left) and after 5 s of braking (right).

GCI: grey cast iron; LC, laser cladding.

distribution throughout the disc thickness, at the instant of 1 s throughout a braking event. Peak temperatures reach 272°C and 320°C for GCI and LC, respectively, therefore 18% higher at the LC surface as opposed to that of GCI. Considering the GCI substrate region of both models (where the disc thickness is between 0 and 10 mm), the GCI model leads the LC by a 5% mean percentage difference in temperature. Temperatures close to the bottom of the disc are of almost negligible differences and close to the initial magnitude (100°C). This constitutes that as expected, 1 s is insufficient for the surface thermal energy of both models to propagate throughout the entirety of the disc.

On the other hand, right of Figure 5 is the thermal distribution at the instant of 5 s, therefore still within braking conditions. Peak temperatures reach 378°C and 409°C for GCI and LC, respectively, hence 8% higher in the LC surface this time. Again comparing both GCI regions ($0 < \text{disc thickness} \leq 10 \text{ mm}$), the GCI model exceeds average LC temperatures by a 4% mean percentage difference. Both plots visibly follow similar temperature gradients, as for the 1 s instant (left graph of Figure 5). By inspection, it can be deduced that both models develop thermal energy in a synchronous manner, with increase in braking time. Nevertheless, GCI still presents higher internal temperatures compared to LC. Moreover, temperature gradients appear to be of almost equal magnitudes for both LC coatings. However, at the interface region of the GCI substrate with the first LC coating (Inconel 718 interlayer), there exists a substantial change in slope. This indicates that the rate of change of temperature, T ($^{\circ}\text{C}$), with disc thickness, δ (mm), is higher within the LC coating as opposed to the GCI substrate ($\left. \frac{\partial T}{\partial \delta} \right|_{\text{LC}} > \left. \frac{\partial T}{\partial \delta} \right|_{\text{GCI}}$). Therefore, the LC buffer layer proves to successfully act as a thermal

barrier, as it decreases the rate of heat beyond its interface region.

Following is a series of stretched volume plots in Figure 6, which are cut at their quarter sections to display the evolving temperature map across their surfaces as well as their interiors. Each column corresponds to time instants of 0.1, 1 and 5 s of braking, and are governed by the same temperature map as indicated in their legends, for clear comparison purposes between GCI (top row) and LC (bottom row). Due to the vertical deformation of the models, for LC (bottom row), the two coating layers can be observed outlined around the top of the disc.

Results demonstrate of being in line with literature data.^{9–11} It can be observed that higher temperatures are attained in the LC coating as opposed to the GCI surface. As expected, differences in material properties of each model constitute clear divergences in thermal behaviour. Thermal conductivity of GCI ($k_{\text{GCI}} = 50 \text{ W}/(\text{m} \cdot \text{K})^9$) is over three times higher to that of AISI 420 ($k_{\text{AISI 420}} = 16 \text{ W}/(\text{m} \cdot \text{K})^{14}$) as the stainless steel exterior coating of LC. The consequence of this is immediately observed throughout the first second of braking, where surface temperatures of LC surpass those of GCI by almost 20%. Due to its lower conductivity, heat dispersion is limited in the stainless steel coating which explains the proportion of thermal energy that differs from GCI. Furthermore, the LC Inconel 718 buffer layer demonstrates to act as a thermal barrier. Its thermal conductivity ($k_{\text{Inconel 718}} = 11 \text{ W}/(\text{m} \cdot \text{K})^{13}$) is 4.5 times inferior to that of GCI, meaning much of the thermal energy is stored in this interlayer instead of being conducted through to the GCI substrate. Plots representing particular time instants, can be linked back those displayed in Figure 5 for clarity. Temperature differences

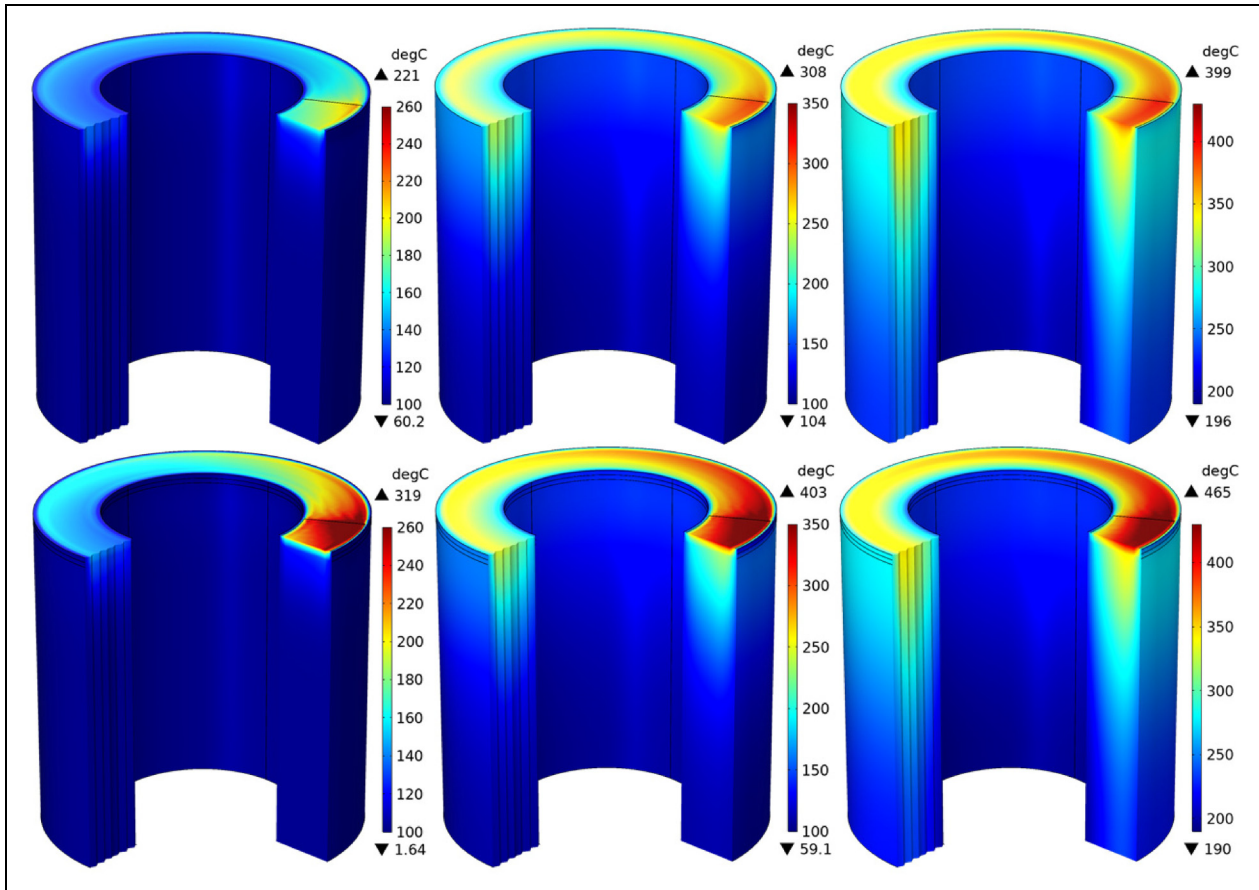


Figure 6. Cross-sectional displays of temperature contour maps for GCI (top row) and LC (bottom row). Time instances are 0.1, 1 and 5 s of braking, corresponding to each column, respectively. Legend units: °C. GCI: grey cast iron; LC, laser cladding.

from the above results are also proven from mass and specific heat capacity quantities of each domain. From the equation:

$$Q = mC_p\Delta T \quad (10)$$

where Q (J) is the supplied thermal energy, m (kg) is the mass of the body, C_p (J / (K · kg)) is the specific heat capacity of the material and ΔT (K) is the temperature change, the following relationship can be made. Given that supplied heat rates of GCI and LC are purely distinguished by the heat partition coefficient (98% for GCI and 97% for LC), for the sake of the comparison, they may be assumed to be equal. Hence, by equating equation (10) to GCI and the LC exterior coating (AISI 420), the following relationships are drawn:

$$mC_p\Delta T|_{\text{GCI}} = mC_p\Delta T|_{\text{LC}} \quad (11)$$

$$\frac{mC_p|_{\text{GCI}}}{mC_p|_{\text{LC}}} = \frac{\Delta T_{\text{LC}}}{\Delta T_{\text{GCI}}} \quad (12)$$

For an inferior mass (of AISI 420 coating as opposed to GCI substrate) and inferior specific heat capacity (10% less in AISI 420 from GCI,^{9,14} see Table 1), the overall products are related by the inequality below. Therefore, the inverse proportionality logically constitutes that the

change in temperature must be greater in the LC model surface, as opposed to GCI:

$$mC_p|_{\text{LC}} < mC_p|_{\text{GCI}} \quad (13)$$

$$\Delta T_{\text{LC}} > \Delta T_{\text{GCI}} \quad (14)$$

It can thus be observed that results from Figures 5 and 6 both follow this relationship successfully. Von Mises stresses can now be obtained from the thermal data, previously computed. Now that temperature comparisons have been made, a thermal stress analysis is studied.

Stress analysis

Figure 7, which displays the stress evolution along the thickness line, demonstrates a range of stresses distinguished between each model. Right of Figure 7 is the zoomed-in view where the coating sections can be identified from the horizontal axis.

The above plots from Figure 7 are obtained owing to computed temperature data previously displayed in Figures 5 and 6. These are plotted at a time instant of 5 s within a braking cycle, hence approaching maximum attained temperatures. Left of Figure 7 is the full disc thickness with corresponding thermal stress values

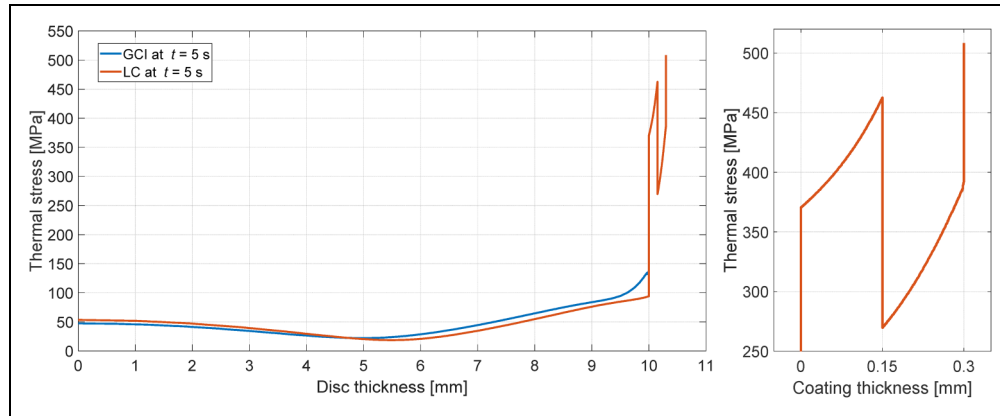


Figure 7. Thermal stress evolution along the disc thickness line for GCI and LC, after 5 s of braking. The full disc thickness is displayed on the x -axis (left). The zoomed in LC coating thickness only, is displayed on the x -axis (right). Looking at ‘Coating thickness’ (right), interface of GCI substrate to Inconel 718 interlayer occurs at 0 mm; interface of Inconel 718 interlayer to AISI 420 overlayer occurs at 0.15 mm; and interface of AISI 420 overlayer to pad contact occurs at 0.3 mm. GCI: grey cast iron; LC, laser cladding.

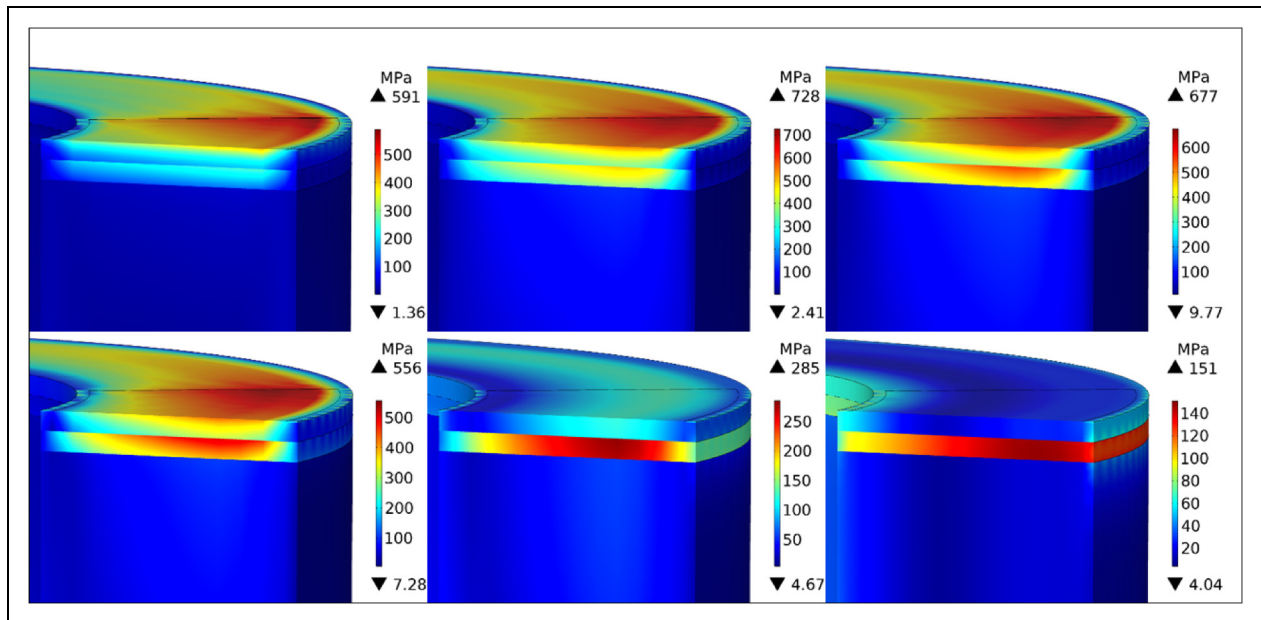


Figure 8. Cross-sectional zoomed-in coating displays of thermal stress contour maps for laser cladding (LC). Time instances are 0.1, 1 and 3 s of braking, from left to right sequentially (top row). Time instances are 5, 6 and 10 s of braking, from left to right sequentially (bottom row). Legend units: MPa.

along it. Visibly, substantial stresses are developed at a thickness of 10 mm, as the interface region of the GCI substrate with the Inconel 718 interlayer. Peak stresses from LC are almost incomparable to those from GCI. It can be observed that thermal stresses of the GCI peak at 137 MPa, which surpasses magnitudes of LC up and until 10 mm. This can be explained by the fact that temperatures at this point in space and time are higher in GCI as indicated right of Figure 5.

Looking right of Figure 7, the LC coating thickness is displayed with zoomed-in peak data to clearly observe thermal stresses. The first LC peak (substrate to Inconel 718 interface) is at 370 MPa, the second LC peak (Inconel 718 to AISI 420 interface) is at 463 MPa and the surface of AISI 420 is at 508 MPa. These peak

values are anticipated given that they occur precisely at each interface between domains (substrate, interlayer and surface layer). Distinct expansion rates are therefore expected from different materials against one another, causing significant thermal stresses within these regions.

Following are a sequence of stretched volume cut displays in Figure 8 for LC. These are cut at their half sections to observe development of stresses zoomed-in at the laser cladded layer interfaces. The sequence is taken for time instances of 0.1, 1, 3, 5, 6 and 10 s, respectively. Each of these hold a different colour range corresponding to the appropriate stress distribution map at that period in time.

These final contour plots from Figure 8 show an evolution of interface stresses, which can be observed at

interface regions with increase in time. The plot which represents a 5 s time instant, can be linked back to the plot displayed in Figure 7 for clarity. It is clear how at 6 s, when the brake pad has been released, surface stresses begin to decrease as the disc is undergoing cooling. Stresses are consequently stored in the interlayer where they require a longer period of time to dissipate. From the relationship below, it can be predicted that thermal stresses within the LC model will significantly surpass those of GCI:

$$\sigma = \alpha E \Delta T \quad (15)$$

where σ (Pa) is the thermal stress, α is the thermal expansion coefficient of the material, E (Pa) is the Young's modulus of the material and ΔT (K) is the temperature change. Thermal expansion coefficients, α , of GCI and AISI 420 are both equal to $11 \mu\text{K}^{-1}$ (see Table 1^{9,14}). Equation (15) can be expressed for both GCI and LC. Hence, the α terms may be equated to relate both these equations:

$$\frac{\sigma}{E \Delta T} \Big|_{\text{GCI}} = \frac{\sigma}{E \Delta T} \Big|_{\text{LC}} \quad (16)$$

$$\frac{\sigma_{\text{LC}}}{\sigma_{\text{GCI}}} = \frac{E \Delta T \Big|_{\text{LC}}}{E \Delta T \Big|_{\text{GCI}}} \quad (17)$$

Therefore, for Young's modulus material data from Table 1 (98 GPa for GCI and 200 GPa for AISI 420) and from previously computed temperature data for both GCI and LC, the following inequality may be stated:

$$E \Delta T \Big|_{\text{LC}} > E \Delta T \Big|_{\text{GCI}} \quad (18)$$

Constituting that thermal stresses from the LC surface coating are superior to those from GCI:

$$\sigma_{\text{LC}} > \sigma_{\text{GCI}} \quad (19)$$

The above results consequently follow this analytical relationship successfully.

Discussion

It is important to highlight that a braking power compensation was insured by adjusting the normal force applied to the LC rotor, in response to friction coefficient differences with GCI. This was in order to satisfy an equal rate of heat flux to both models, where differences were purely influenced by variations in heat partition coefficients. Therefore, a coherent comparison can be drawn from the obtained results of each model.

Regarding thermal performance, GCI does in fact seem to infiltrate more heat into the body of the disc as opposed to LC. It is also clear through the comparison that the coating creates an extremely localised temperature at the surface, observed by the steep gradient that peaks once the nickel-based alloy interlayer is reached.

Reasons for this high temperature peak at the LC surface relate back to the fact that the surface material, martensitic stainless steel has a lower thermal

conductivity meaning it is less capable of diffusing heat across it, as well as the underlayer which introduces a visibly steep temperature gradient. This also demonstrates that the nickel-based alloy inter-layer performs as a thermal barrier resulting from its low conductivity and diffusivity. Therefore, as overall conduction is lower, LC stores more thermal energy at the upper surface where the pad-disc contact occurs. However, it is crucial to take into consideration that the coefficient of heat partition of the LC surface is 97% (as opposed to 98% for GCI), meaning 1% more of the generated heat is being conducted through to the friction material of the pad. The thermal properties of the friction material must be re-evaluated in order to determine the safety threshold temperatures that it could withstand without a negative influence in braking performance such as brake fade.

Now looking into thermal stress performance for LC, it is visible how significant peaks are developed at each interface layer of the laser clad coating, whereas the remaining interior of the disc is not experiencing a significant stress magnitude. This compares very clearly to GCI that displays again a very gradual development of stresses reaching a maximum at the disc extremity. As has been expected consequently, boundaries of the laser clad layers experience very high thermal stresses due to the fact that they act as constraints to each other, impeding their volumetric thermal expansion as their internal energy increases. Different rates of heat being received by different materials, each with different thermal expansion coefficients therefore introduces a very significant risk when it comes to the LC deposition. Due to its highest expansion coefficient value from the three materials and as the layer constrained by both its upper and lower interfaces,⁵ the nickel-based alloy inter-layer is therefore experiencing the highest level of thermal stresses. Therefore, the LC process must be done with extra care in the deposition procedure, in order to correctly align the thermal expansion magnitudes⁵ to those which best satisfy the stress predictions at bonding regions.

In summary, the temperature field has demonstrated that LC is capable of generating much higher temperatures than GCI. Its higher friction coefficient introduces a stronger and more reliable braking performance and heat infiltration is minimised with respect to the range of overall generated temperatures. This combination of bonded materials brings about a different distribution of thermal energy as opposed to a conventional GCI disc model.

The stress field on the other hand has studied the constraint requirements that an LC model must be able to withstand for it to be successfully implemented. Hence, high developed stresses occur at the layer interfaces¹⁵ which challenges the LC application process in optimising the metallurgical bonding and layer deposition. Accuracy techniques must be re-evaluated to determine a specific bonding tolerance that could be compared to modelled results.

An analysis of mechanical stresses must be conducted in order to determine load capabilities and the capacity of withstanding very high rotational shear stresses. Frictional forces which translate into rotational shear would, therefore, need to prove that the rotor compound is able to withstand the mechanical stresses associated with different stages of braking.

It is important to note that this project has analysed purely transient regimes, i.e. where inward and outward fluxes have been dominant in the studied time period.¹⁶ The laser cladded performance should also be evaluated under steady-state scenarios such as in the case of a pin-on-disc tribometer where the input heat equals the output dissipation.⁴ Time, gradient and steady-state level comparisons would offer another clear investigation into the reliability of the coating.

The research was also made to simulate an experimental performance made at room temperature, where the rotor was also set to perform at temperatures ≥ 100 °C.⁹ It would therefore be crucial to evaluate performances under a range of temperature scenarios. These may include temperatures <0 °C, or being subject to moisture and water from rain or humidity. The contrast in rotor temperatures would hence introduce a performance prediction to thermal shocks. In this scenario, laser cladded rotors may serve to be highly beneficial as opposed to conventional rotors, however, this may introduce a more demanding thermo-structural degree of freedom.

Limitations of the study can be linked to a potential lack of surface topography detail. Therefore, as to what concerns surface texture, experimental iteration should be done to study the extent to which surface topography affects the tribological performance of braking.¹⁷ If a significant influence is detected, such an effect would need to be implemented to improve the overall experimental validation of the model. Moreover, regarding parameters, a more accurate experiment would require evolving magnitudes of material data influenced by temperature changes. Thermal softening would provide the corresponding set of parameters for every temperature level such as a decrease in Young's modulus. As well as this, mean coefficient of friction values were used, inputted as constant parameters which were retrieved from experimental results.^{6,9} In a real case scenario, the friction coefficient evolves throughout a braking event in response to contact pressure variations and plateau dynamics.⁹ Experimental recordings of friction coefficient values from pin-on-disc setups could be fed back into the simulation model even in the form of fluctuations for improvement. The FEA model would also benefit from more accurate and realistic convective heat transfer coefficient values.¹⁸ Its validation would be optimised through a computational fluid dynamic study, by recreating the experimental setup.¹⁶

Furthermore, it should be noted that for simplicity, heat flux distribution was assumed as being uniform. This limitation must be acknowledged given that non-uniformity due to transient regimes, constitute local hot spots in contact regions from focal heating.^{17,19} Considering

plateaus to implement non-uniform contact pressures would provide a more realistic heat-flux distribution.²⁰ In addition, it must be said that maximum surface temperatures are also highly influenced by the heat partition coefficient which in reality, is not a static quantity.²⁰ It is dependent on temperature as well as contact pressure distribution, which evidently vary with time throughout a braking event. Given that dynamic modelling of the heat partition coefficient is particularly complicated,²¹ simplicity was hence achieved using that proposed by Vernotte.¹² Hasselgruber,²² Ginzburg,²³ and Charron²⁴ have also proposed different forms of determining heat partition coefficients which future simulations would benefit from.

Regarding the FEA model itself, there is no presence of the pad component. In consideration, its only influence is regarding the heat partition coefficient, ξ . To take the simulation model further, a CAD assembly should be used with mating components (pad and disc) as opposed to a single component system. This should allow the evaluation of the pad performance, in response to an LC integration.

Therefore, the simulation model can be used for future optimisation and validation development, with the use of experimental data from LC rotors. By recreating the described scenario in a dynamometer test, full-scale experimental validation would be achieved.

Conclusions

Temperature and mechanical performance were investigated by the use of FEA modelling using COMSOL Multiphysics 5.6. A comparison was made between a laser cladded disc and a conventional homogeneous GCI disc. These models were primarily distinguished by the laser cladded model consisting of a material combination involving a nickel-based alloy interlayer and martensitic stainless steel overlayer surface. A highly simplified and computational cost-effective FEA model was delivered. The summarised conclusions were drawn as follows:

- Meshing of the LC coating and GCI substrate is easily and effectively achieved, at reduced computationally cost, to validate interior temperature and thermal stress data of the FEA model, using the given mesh combination.
- The LC nickel-based alloy interlayer proves to act as a thermal obstructer to temperatures infiltrating the GCI substrate.
- Peak surface temperatures of LC attain 18% higher values as opposed to GCI, within the first second of braking. This peak temperature difference decreases over further braking time.
- The LC interlayer (Inconel 718) presents difficulty in effectively dissipating thermal stresses from its domain even after the brake pad is released from the disc.

- Peak thermal stresses of LC reach values which are 3.7 times those of GCI after 5 seconds of braking.
- For a 5 s braking event using an LC model, thermal stresses reach magnitudes superior to 450 MPa at the nickel-based alloy interlayer and superior to 500 MPa at the martensitic stainless steel over-layer surface.

Acknowledgements

The authors are grateful for the contributions provided by Fabrizio Girolimetti on simulation development.



Declaration of Conflicting Interests

The authors declared no potential conflicts of interest with respect to the research, authorship and/or publication of this article.

Funding

The authors received no financial support for the research, authorship and/or publication of this article.

ORCID iDs

Nicholas Athanassiou  <https://orcid.org/0000-0002-1577-5605>
Jens Wahlström  <https://orcid.org/0000-0003-0696-7506>

References

1. Alemani M. *Particle emissions from car brakes: The influence of contact conditions on the pad-to-rotor interface*. PhD Thesis, KTH Royal Institute of Technology, Sweden, 2017.
2. Air Quality Expert Group. Non-exhaust emissions from road traffic, https://uk-air.defra.gov.uk/assets/documents/reports/cat09/1907101151_20190709_Non_Exhaust_Emissions_typeset_Final.pdf (2019, accessed 5 June 2020).
3. Federici M. *Study of wear mechanisms in braking systems with HVOF-coated discs*. PhD Thesis, University of Trento, Italy, 2019.
4. Wahlström J, Lyu Y, Matjeka V, et al. A pin-on-disc tribometer study of disc brake contact pairs with respect to wear and airborne particle emissions. *Wear* 2017; 384–385: 124–129.
5. Qi K, Yang Y, Hu G, et al. Thermal expansion control of composite coatings on 42CrMo by laser cladding. *Surf Coat Technol* 2020; 397: 2–4.
6. Dizdar S, Lyu Y, Lampa C, et al. Grey cast iron brake discs laser clad with nickel-tungsten carbide—friction, wear and airborne wear particle emission. *Atmosphere* 2020; 621: 1–11.
7. Martawirya S, Ramdan RD, Prawara B, et al. Mechanical properties, microstructure and wear characteristic of abrasible material coated by HVOF with variation of surface treatment and spray distance. In: *1st international seminar on advances in metallurgy and materials (i-SENAMM 2019)*, Jakarta, Indonesia, 12–13 December 2019, paper no. 060010, pp.1–5.
8. Müller M and Ostermeyer GP. A cellular automation model to describe the three-dimensional friction and wear mechanism of brake systems. *Wear* 2007; 263: 1175–1188.
9. Wahlström J. A comparison of measured and simulated friction, wear, and particle emission of disc brakes. *Tribol Int* 2015; 92: 503–511.
10. Pan G and Cai R. Thermal stress coupling analysis of ventilated disc brake based on moving heat source. *Adv. Mater Sci Eng* 2018; 2018: 1–11.
11. Spulber C and Voloaca S. Comparison between some simulation methods regarding the thermal stress on disc brake. *Appl Mech Mater* 2013; 325–326: 135–141.
12. Vernotte P. *Thermocinétique générale*. 1st ed. Paris: Publications Scientifiques et Techniques du Ministère de l'air (379), 1961.
13. MAHER. Data sheet. Alloy 718, February 2020.
14. UDDEHOLM. Data sheet, UDDEHOLM STAVAX ESR, May 2013.
15. Belhocine A. FE prediction of thermal performance and stresses in an automotive disc brake system. *Int J Adv Manuf Technol* 2016; 89: 3564–3574.
16. Belhocine A and Bouchetara M. Investigation of temperature and thermal stress in ventilated disc brake based on 3D thermomechanical coupling model. *Ain Shams Eng J* 2013; 4: 475–483.
17. Rabinowicz E. Influence of surface energy on friction and wear phenomena. *J Appl Phys* 1961; 32: 1440–1444.
18. Lyu Y and Olofsson U. On black carbon emission from automotive disc brakes. *J Aerosol Sci* 2020; 148: 1–4.
19. Guo YB, Zhang Z, Zhang QL, et al. Tribological characteristics of W2C reinforced Mn copper-nickel alloy matrix composite coating for rig disc brake. *Surf Topogr Metrol Properties* 2019; 7: 3–11.
20. Tarasiuk W, Golak K, Tsybrii Y, et al. Correlations between the wear of car brake friction materials and airborne wear particle emissions. *Wear* 2020; 456–457: 1–9.
21. Loizou A, Hong-Sheng QI and Day AJ. Analysis of heat partition ratio in vehicle braking processes. In: *Braking 2009: institution of mechanical engineers, automobile division conference*, London, UK, 9–10 June 2009.
22. Hasselgruber H. Der schaltvorgang einer trockenreibung kupplung beikleinster erwärmung. *Konstruktion* 1963; 15: 41–45.
23. Ginzburg AH. Theoretical and experimental bases for calculation of unitary process of braking by means of system of the equations of thermal dynamics of friction. *Nauka* 1973: 93–105.
24. Charron F. *Partage de la chaleur entre deux corps frottants*. 1st ed. Paris: Publications scientifiques et techniques du Ministère de l'air (182), 1943.